Bond ordering and molecular spin-orbital fluctuations in the cluster Mott insulator GaTa$_4$Se$_8$

Tsung-Han Yang ®,[1] S. Kawamoto ®,[2] Tomoya Higo ®,[3] SuYin Grass Wang,[4] M. B. Stone ®,[5] Joerg Neuefeind ®,[5]
Jacob P. C. Ruff,[6] A. M. Milinda Abeykoon,[7] Yu-Sheng Chen,[4] S. Nakatsuji,[2,3,8,9] and K. W. Plumb ®[1]

[1]*Department of Physics, Brown University, Providence, Rhode Island 02912, USA*
[2]*Institute for Solid State Physics, University of Tokyo, Kashiwa, Chiba 277-8581, Japan*
[3]*Department of Physics, The University of Tokyo, Tokyo 113-0033, Japan*
[4]*NSF's ChemMatCARS Beamline, The University of Chicago, Advanced Photon Source, Argonne, Illinois 60439, USA*
[5]*Neutron Scattering Division, Oak Ridge National Laboratory, Oak Ridge, Tennessee 37831-6573, USA*
[6]*Cornell High Energy Synchrotron Source, Cornell University, Ithaca, New York 14853, USA*
[7]*Photon Sciences Division, Brookhaven National Laboratory, Upton, New York 11973, USA*
[8]*Institute for Quantum Matter and Department of Physics and Astronomy, The Johns Hopkins University, Baltimore, Maryland 21218, USA*
[9]*Trans-scale Quantum Science Institute, University of Tokyo, Tokyo 113-0033, Japan*

For materials where spin-orbit coupling is competitive with electronic correlations, the spatially anisotropic spin-orbital wave functions can stabilize degenerate states that lead to many and diverse quantum phases of matter. Here we find evidence for a dynamical spin-orbital state preceding a $T^* = 50$ K order-disorder spin-orbital ordering transition in the $j = 3/2$ lacunar spinel GaTa$_4$Se$_8$. Above T^*, GaTa$_4$Se$_8$ has an average cubic crystal structure, but total scattering measurements indicate local noncubic distortions of Ta$_4$ tetrahedral clusters for all measured temperatures $2 < T < 300$ K. Inelastic neutron-scattering measurements reveal the dynamic nature of these local distortions through symmetry forbidden optical phonon modes that modulate $j = 3/2$ molecular orbital occupation as well as intercluster Ta-Se bonds. Spin-orbital ordering at T^* cannot be attributed to a classic Jahn-Teller mechanism and, based on our findings, we propose that intercluster interactions acting on the scale of T^* act to break global symmetry. The resulting staggered intercluster dimerization pattern doubles the unit cell, reflecting a spin-orbital valence bond ground state.

I. INTRODUCTION

It is a maxim of condensed matter physics that the many and varied properties of strongly correlated materials arise from an intricate interplay of spin, orbital, and lattice degrees of freedom. Often, the spin and orbital degrees of freedom have a mutual influence, but can be treated as distinct energy scales. Static orbital configurations impart a spatial anisotropy to affect many and diverse magnetic phenomena. For instance, orbital ordering can influence magnetic exchange interactions to generate magnetic frustration in nominally unfrustrated lattices [1] or relieve magnetic frustration and drive valence bond solid transitions in frustrated magnets [2–4]. Orbital overlap in metals can create one-dimensional bands in nominally three-dimensional materials. The resulting Peierls instability on those bands generates intricate superstructures of spin singlets on structural dimers through an orbitally induced Peierls mechanism [5–7].

Both relativistic spin-orbit coupling and covalency can act to reduce the separation of spin and orbital energy scales, enabling quantum fluctuations between nearly degenerate states. In the extreme limit of large spin-orbit coupling orbital degeneracy is either partially or totally removed depending on the electron filling. For instance, for a single electron occupying a t_2 orbital triplet, spin orbit coupling stabilizes a total $j = 3/2$ quartet where the resulting spin-orbital wave functions alter Jahn-Teller potentials to promote fluctuations among many possible structural distortions [Fig. 1(a)] [8]. Such spin-orbital degrees of freedom naturally support spatially anisotropic and higher order, multipolar exchange interactions [9–11]. Covalency plays a similar, but lesser explored, role to reduce the tendency toward classical Jahn-Teller distortions in solid state materials [12–14]. Typically, the effective strength of spin-orbit coupling is reduced in covalent materials, but, in materials where small clusters of atoms hybridize to form molecular units, the effects can be competitive. In such cluster Mott insulators, the interplay of orbitals, magnetism, and spin-orbit coupling on the molecular clusters leads to many diverse possibilities [15].

In this work, we use x-ray diffraction, total scattering, and neutron spectroscopy to reveal dynamic spin-orbital fluctuations preceding a spin-orbital ordering transition in the $j = 3/2$ cluster Mott insulator GaTa$_4$Se$_8$. At high temperatures, we find an average cubic crystal structure, but local cubic
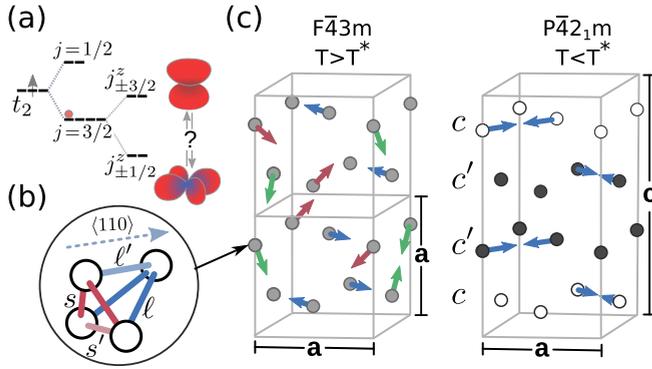
FIG. 1. Unit cell doubling and intercluster dimers in GaTa$_4$Se$_8$. (a) Spin-orbit coupling driven $j = 3/2$ states on Ta$_4$ cluster molecular orbitals. j^z spin-orbital states are Jahn-Teller degenerate. (b) Monoclinically distorted Ta$_4$ clusters with four inequivalent Ta-Ta distances $\ell > \ell' > s' > s$ point along local $\langle 110 \rangle$ axis. (c) Local distortions of Ta$_4$ clusters on FCC lattice fluctuate among $\langle 110 \rangle$ directions for $T > T^*$, shown as colored arrows. Intercluster interactions select a global rotational symmetry breaking below T^*. Unit cell doubling occurs through a formation of two inequivalent Ta$_4$ stacked in a c-c'-c'-c pattern.

symmetry is dynamically broken on Ta$_4$ clusters for all measured temperatures, $T \leqslant 300$ K. The Ta$_4$ clusters distort along local $\langle 110 \rangle$ directions and fluctuate incoherently in space and time (Fig. 1). Global symmetry is broken at $T^* = 50$ K as clusters coherently align toward a single neighboring cluster through a collective spin-orbital ordering transition. The distorted clusters exhibit an antiferro configuration doubling the cubic unit cell in a bond ordered structure as illustrated in Fig. 1(c). Inelastic neutron-scattering measurements directly resolve the fluctuations associated with the disordered state above T^* through the appearance of symmetry forbidden optical phonon intensity. These lattice fluctuations are a manifestation of the dynamic spin-orbital state arising from a highly degenerate potential. We propose that intercluster spin-orbital exchange interactions act to break the degeneracy at T^* and stabilize a long-range spin-orbital order in GaTa$_4$Se$_8$.

GaTa$_4$Se$_8$ belongs to a family of cluster Mott insulating lacunar spinels with chemical formula GaM$_4$X$_8$, M = (V, Mo, Nb, Ta), X = (S, Se) [16–24]. The essential structural units are cubane (M$_4$X$_4$)$^{5+}$ clusters that occupy an FCC lattice. For M = (V, Nb, Ta), a single unpaired electron is localized on the cubane tetrahedral transition metal clusters. The transition metal atomic orbitals hybridize across M_4 clusters to form molecular orbital wave functions with the highest occupied molecular orbitals on a tetrahedron composed of triply degenerate t states as shown in Fig. 1(a) [18]. As a consequence of the Jahn-Teller active molecular orbital, many of the lacunar spinels exhibit a typical separation of spin and orbital energy scales whereby a high-temperature cooperative Jahn-Teller, orbital ordering, structural transition precedes a lower-temperature magnetic ordering [17,19,20]. However, in those compounds with heavy transition metals (Nb, Ta), such a separation of spin and orbital energy scales is either drastically diminished or does not exist [18,25,26]. For both GaTa$_4$Se$_8$ and GaNb$_4$S$_8$, the spatial extent of transition metal

wave functions and strong atomic spin-orbit coupling act to control the ground states and a single temperature scale T^* defines magnetic and structural transitions [18,27,28].

The importance of spin-orbit coupling in GaTa$_4$Se$_8$ is borne out through density-functional theory (DFT) and resonant inelastic x-ray scattering that suggest the molecular orbitals form a spin-orbit entangled $j = 3/2$ quartet [Fig. 1(a)], analogous to the case of octahedrally coordinated d^1 Mott insulators [29–31]. Such $j = 3/2$ spin-orbit entangled molecular orbitals are consistent with the reported small paramagnetic moment and entropy released at T^* [26,27]. In this case, the magnetic ground state below T^* is formed from spin-orbital singlets as predicted for $j = 3/2$ on an FCC lattice [10,11] with profound implications for the electronic properties of GaTa$_4$Se$_8$. Above T^* and at ambient pressure, GaTa$_4$Se$_8$ is a strongly correlated insulator, but it exhibits an insulator to metal and superconducting transition under the application of hydrostatic pressure [18,32,33]. Molecular $j = 3/2$ degrees of freedom would support a topological superconducting state at high pressure [31,34]. However, the $j = 3/2$ quadruplet on t_2 orbitals is also Jahn-Teller active. For atomic $j = 3/2$ insulators, spin-orbit coupling acts to suppress Jahn-Teller distortions and, to first order, octahedral compression and elongation provide equal energy gain. This additional degeneracy results in a nonadiabatic "Mexican hat" potential energy surface that promotes quantum fluctuations among different distortions [8]. Weak lattice anharmonicity or additional electronic interactions, may then act to ultimately select a distortion that is different from what a conventional Jahn-Teller effect would predict. A similar situation may apply to the molecular orbitals of GaTa$_4$Se$_8$; however, currently the low-temperature crystal structure is unknown and there is little information on the spin-orbital configuration below T^*.

There is indirect evidence for a magnetic singlet, valence bond solid like, ground state from neutron diffraction, μSR, and NMR [26,27]. However, there is no information about the actual valence bond covering on the highly frustrated on the FCC lattice of GaTa$_4$Se$_8$ and limited understanding of the intercluster interactions that might generate such spin-orbital singlets across molecular orbitals. Furthermore, expectations of strong Ta-Se covalency and configurational mixing not captured by DFT bring the $j = 3/2$ picture into question [35–37]. Given the strong connection between the spin, orbital, and lattice degrees of freedom and the lattice, a detailed account of the evolution of the lattice through T^* is essential to understand the low-temperature electronic state and it's relation to high pressure superconductivity in GaTa$_4$Se$_8$.

II. X-RAY CRYSTALLOGRAPHY AND UNIT CELL DOUBLING

GaTa$_4$Se$_8$ has a single magnetic and structural transition at $T^* = 50$ K where the magnetic susceptibility abruptly drops and the unit cell doubles, as indicated by the sudden appearance of structural superlattice Bragg reflections at [1/2, 0, 0] positions [Fig. 2(a)]. As shown in Figs. 2(b) and 2(c), a bifurcation of cubic [h, 0, 0] reflections and abrupt volume decrease at T^* indicate a first-order cubic to tetragonal transition, but with no detectable hysteresis or phase coexistence. Above T^*, single crystal XRD consistently refines to the
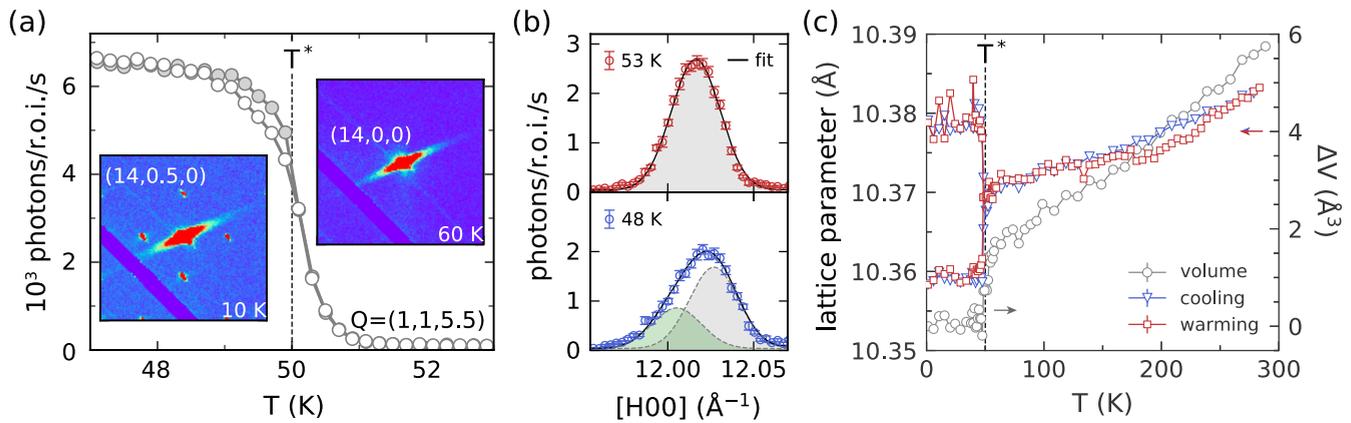
FIG. 2. (a) X-ray diffraction reveals a first-order onset of superlattice [1/2, 0, 0] at T^*. (b) Bifrucation of [12,0,0] reflection at T^* indicating a low-temperature tetragonal cell. (c) Temperature dependence of lattice parameter and cell volume extracted from the [12,0,0] reflection. There is a sharp decrease in volume at T^* but no measurable hysteresis.

cubic space group F$\bar{4}$3m. Below T^*, the [1/2, 0, 0] reflections indicate a unit cell doubling along a unique cubic axis and we observed all [1/2, 0, 0] reflections consistent with six domains of the tetragonal cell. We did not find any additional peak splitting or evidence for an orthorhombic distortion. We have evaluated our $T = 10$ K single crystal XRD data against all subgroups of the cubic cell that are consistent with a $k = [1/2, 0, 0]$ distortion; body centered space groups are ruled out by the observation of reflections with $h + k + l \neq 2n$ and based on the absence of any $[2n + 1, 0, 0]$ reflections we ruled out all possible primitive groups except for $P\bar{4}2_1m$, more details are described in Appendix B.

We obtain high-fidelity refinements for P$\bar{4}2_1$m with $a = b = 10.3437$ and $c = 20.6878$ ($R_1 = 0.0879$ for 13 104 reflections). Within the tetragonal cell there are two distinct Ta$_4$ clusters labeled c and c' in Fig. 1(c), each having the same symmetry, but different Ta-Ta bond lengths. The symmetry of tetrahedral clusters is reduced to monoclinic and retains a single mirror plane. Each cluster contains four different bond lengths shown in Fig. 1(b) and listed in Table I, with three long bonds, labeled ℓ and ℓ' ($\ell > \ell'$), and three short-bonds labeled s and s' ($s < s'$) resulting in a characteristic elongation of tetrahedra along cubic *face diagonals*. Each Ta$_4$ cluster points along $\langle 110 \rangle$ toward a single neighboring cluster, forming an intercluster dimer motif as illustrated [Figs. 1(b) and 1(c)]. The cubic unit cell doubling occurs through a c-c'-c'-c stacking arrangement of Ta clusters along the c axis, giving rise to [1/2, 0, 0] reflections from six domains of the tetragonal cell.

The structural transition in GaTa$_4$Se$_8$ is distinct from reports in other lacunar spinels. For Ga(V,Nb)$_4$(S,Se)$_8$, the Jahn-Teller active M$_4$ clusters undergo a rhombahedral distortion, displacing along the cubic *body diagonals*, in a fer-rodistortive pattern for vanadium based compounds [17,38–41] and antiferrodistortive pattern for the niobium compounds [20,28]. A primary mode analysis GaNb$_4$S$_8$ found a single Jahn-Teller active mode within irreducible representation X_5 and dominated by displacements of the Nb$_4$ tetrahedra [28]. In contrast, we find that the distortion in GaTa$_4$Se$_8$ is described by a superposition of modes within many irreducible representations. The most dominant distortions belong to X_5

(subgroup P$\bar{4}2_1$m, amplitude = 0.12 Å) and X_3 (subgroup P$\bar{4}$m2, amplitude = 0.07 Å) representations, both modes in-volving nearly equivalent displacements of Ta and Se atoms [42–44]. Unit cell doubling is affected through a combina-tion of W_4 and Δ_1 modes with amplitudes of 0.02 Å and nearly equivalent Ta/Se displacements [44]. Thus, we cannot attribute the transition in GaTa$_4$Se$_8$ to a classic Jahn-Teller mechanism acting through a single normal mode of the cell. The intercluster dimer motif, unit cell doubling, mode mixing, and equivalent contributions from displacements of metal and ligand ions implicates the complex spin-orbital wave function and a mechanism likely involving intersite interactions, are at play in GaTa$_4$Se$_8$.

III. LOCAL DISTORTIONS AND DYNAMIC ORBITAL DEGENERACY BREAKING

Having established the low-temperature space group in GaTa$_4$Se$_8$, we now turn to atomic pair distribution analy-sis (PDF) to provide detailed insight into the evolution of atomic correlations across different length-scales through T^*. Temperature-dependent x-ray (xPDF) and neutron (nPDF) PDF measurements shown in Fig. 3 provide a histogram of atomic pair correlations from which atomic pair separations can be read off independent of a specific structural model. The PDF data for GaTa$_4$Se$_8$ have two striking features. First, the double-peak structure around 3 Å indicates at least two intercluster Ta-Ta distances between 2.9 and 3.1 Å for tem-peratures up to 300 K. Thus, the local crystal structure of GaTa$_4$Se$_8$ is not cubic well into the temperature regime where the average structure is cubic. Second, nPDF and xPDF data do not show any discernible qualitative changes across all measured temperatures beyond thermal broadening. The ab-sence of any change in the local structure is highlighted in Fig. 3(c) that shows a negligible difference in nPDF across T^* and in Fig. 3(d) that shows the normalized PDF peak intensities for inter- and intracluster pair separations

$$x(r', T) = \frac{G(r', T) - G(r', 300)}{G(r', 5) - G(r', 300)}, \quad (1)$$
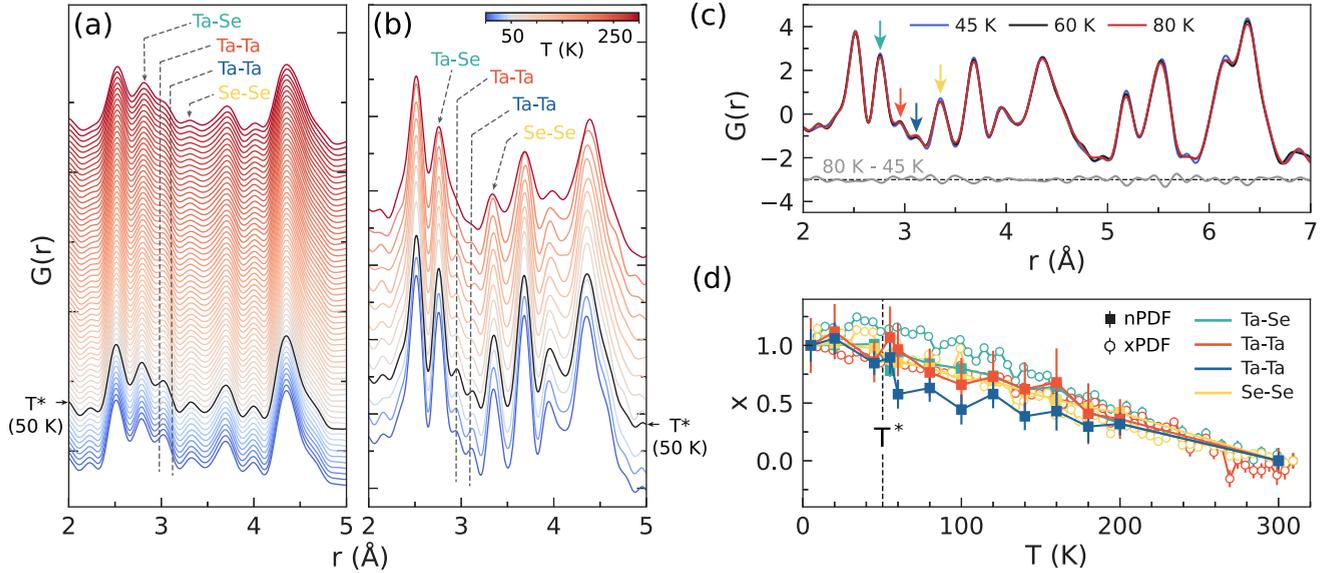
FIG. 3. Temperature dependence of atomic pair separation in $GaTa_4Se_8$. (a) Temperature-dependent xPDF and (b) nPDF measurements show local distortions of Ta_4 clusters exist well above the transition through two distinct intercluster Ta-Ta distances, $s = 2.95$ Å and $\ell = 3.06$ Å observed at all measured temperatures. Real space resolutions of PDF data are $\delta r = 0.233$ Å for xPDF and $\delta r = 0.182$ Å for nPDF. (c) Detailed comparison of small r nPDF above and below T^*. The 45–80 K difference data show no measurable change in atomic pair displacements through the transition. (d) Temperature dependence of normalized inter-Ta_4 cluster PDF peak intensities x showing the continuous and smooth evolution of atomic distances with temperature. Filled symbols are from nPDF and open from xPDF.

where $G(r, T)$ is the PDF intensity at distance r. x acts as an effective local order parameter for displacive transitions [45]. The smooth evolution of x with temperature for all pair separations is consistent with thermal disorder (Debye-Waller) and directly implicates an order-disorder transition at T^*. Local distortions in $GaTa_4Se_8$ are present but uncorrelated across length scales beyond one unit cell at least up to 300 K. At T^*, global cubic symmetry is broken as the distorted units select a unique $\langle 110 \rangle$ axis and stack in a c-c'-c'-c, forming the cell doubled tetragonal structure of Fig. 1(b).

In Fig. 4, we show a model-dependent analysis of the PDF data, covering broad length and temperature scales. A cubic model fails to account for the observed local structure ($r < 5$ Å) for all measured temperatures $T < 300$ K. In particular, the cubic structure cannot capture the two Ta-Ta distances around 3 Å and overestimates the PDF weight for Se-Se pairs at 3.5 Å. This local structure is reproduced at all measured temperatures by the tetragonal $P\bar{4}2_1m$ lattice that includes four intercluster Ta-Ta bond lengths $\ell > \ell' > s' > s$. Within the accuracy of our measurements, the degree of local distortion in $GaTa_4Se_8$ as measured by the bond length difference $\ell - s$ does not depend on temperature, indicating local distortions of Ta clusters are fully set in up to at least $T = 300$ K. On the other hand, the PDF data for $r > 5$ Å are equally well described by the cubic and tetragonal models at all temperatures because the tetragonal cell is metrically cubic ($c/2 \sim a$). We find that within experimentally achievable resolution, the average structures of cubic and tetragonal cells are only distinguished in a PDF measurement through a small anomalous upturn in thermal parameters upon cooling through T^*. Details are described in Appendix C.

Ta_4 tetrahedral clusters in $GaTa_4Se_8$ are distorted at all measured temperatures, indicating that local, and potentially

dynamic, Jahn-Teller distortions are already present at 300 K. Local distortions preceding an orbital ordering structural transition are common in transition metal compounds, but global symmetry breaking is generally also apparent in total scattering measurements through the appearance of a new length scale or an abrupt change in bond lengths as atoms displace through the transition [5,6,45–50]. The structural transition in $GaTa_4Se_8$ is unique in this respect. An absence of any detectable redistribution in PDF intensity though T^* demonstrates that no length scale, or further local symmetry breaking, is introduced at the structural transition on the scale of our measurements. Instead, a global sixfold discrete rotational symmetry breaking occurs at T^*, where already distorted Ta_4 clusters select a particular $\langle 110 \rangle$ axis [Fig. 1(b)]. Superlattice reflections in a diffraction measurement are a consequence of this global rotational symmetry breaking.

IV. PHONON DENSITY OF STATES AND DYNAMIC DISTORTIONS

The energy integrated diffraction measurements presented above find an average cubic structure for $GaTa_4Se_8$ at $T > T^*$, implying that local distortions are incoherently fluctuating in space, time, or both. In Fig. 5 we show the measured phonon density of states (PDOS) as a function of temperature that provide direct evidence for the dynamic nature of local distortions above T^* through the appearance of a symmetry forbidden optical phonon mode (13 meV) well into the cubic phase.

Measured PDOS at select temperatures are shown in Fig. 5(a). The most striking feature of this data is a temperature-dependent 13-meV phonon intensity appearing above background below $T = 200$ K. This mode is visible
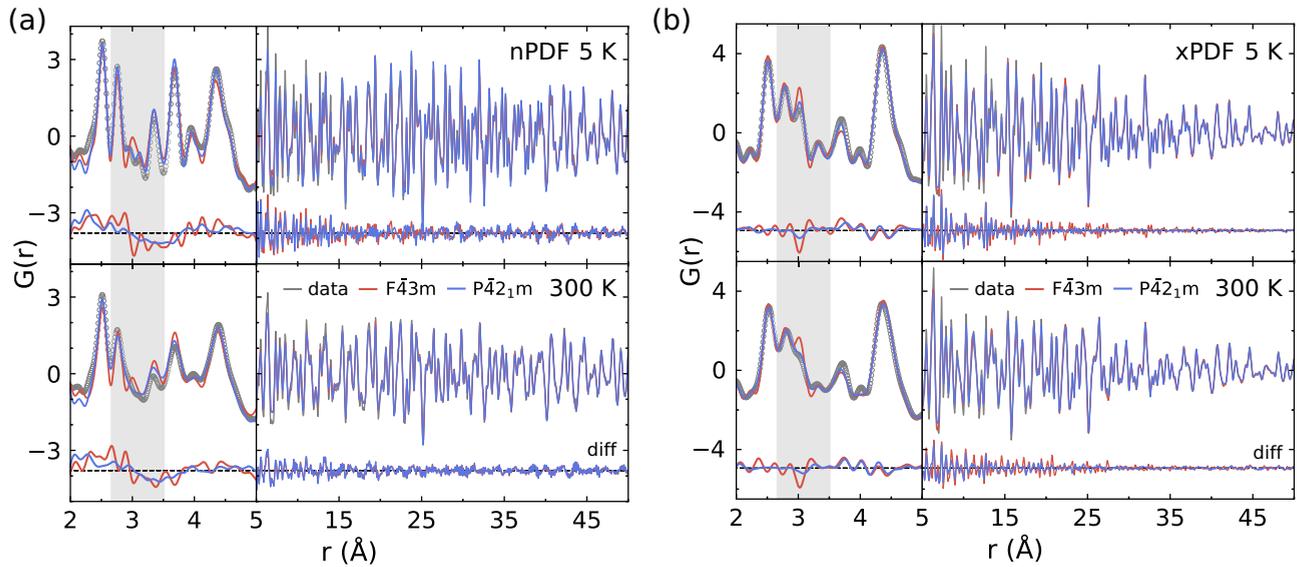
FIG. 4. Local and average structures of $GaTa_4Se_8$. Model fits to neutron pair distribution function measurements at $T = 5$ K and $T = 300$ K for (a) nPDF and (b) xPDF. At all temperatures the tetragonal cell ($P\bar{4}2_1m$) with distorted tetrahedra provides a significantly improved description of the local structure for $r < 5$ Å, while the average structure is equally well described using the cubic or tetragonal cell.

in the raw neutron-scattering data as a nondispersive feature with an intensity that increases quadratically with momentum transfer, ruling out a magnetic origin (see Appendix D). In Fig. 5(c) we show the temperature-dependent integrated intensity of the 13-meV mode, corrected for the Bose factor, and normalized to it's intensity at $T = 10$ K. Above 200 K it was not possible to reliably resolve the 13-meV intensity from the adjacent modes at 10 and 15 meV. We find that the integrated intensity increases linearly with decreasing temperature from 200 K and saturates at T^* while the energy position and width are constant and set by the energy resolution of the spectrometer (see Appendix D). We have carried out first principles calculations of the neutron weighted PDOS for $GaTa_4Se_8$ in order to obtain insight into the origin of the 13-meV intensity. The results of these calculations for both $F\bar{4}3m$ and $P\bar{4}2_1m$ space groups are shown in Fig. 5(b) and are in excellent agreement with the measured spectra. There is a notable absence of phonon modes around 13 meV for the cubic cell; but, significant 13-meV PDOS weight arising from optical phonons in the tetragonal cell. Indeed, the 13-meV phonon intensity is the primary qualitative distinction between the cubic and tetragonal PDOS. The appearance of this optical phonon intensity for $T > T^*$, where the average structure is cubic, directly reflects the dynamic structural fluctuations associated with the local symmetry breaking for $T > T^*$ in $GaTa_4Se_8$ as schematically illustrated in Fig. 1(b). We have evaluated the partial contributions of Ga, Ta, and Se to the PDOS of the tetragonal cell and find the dominant contribution is from Se with additional secondary contributions from Ta and Ga [Fig. 5(b)]. Optical A_1, A_2, B_1, B_2, and E phonon modes all contribute the PDOS between 12 to 14 meV and our data are not consistent with the assignment of a unique Jahn-Teller phonon mode on Ta_4 clusters to this feature of the PDOS.

It is instructive to compare the temperature-dependent phonon spectra in $GaTa_4Se_8$ measured by INS with that measured by infrared spectroscopy (IR). The PDOS as measured by INS contains the full spectrum of predicted vibrational modes, while IR measurements only find a subset of the symmetry allowed modes all attributed to vibrations on the ligand sites [51]. Such a discrepancy must arise as a result of a substantial screening of vibrational modes from electron delocalization over Ta_4 tetrahedral units in insulating $GaTa_4Se_8$. Neutrons interact directly with nuclear cores and are not subject to electronic screening. Such an electronic delocalization is most apparent in $GaTa_4Se_8$ because of the spatially extended nature of Ta d orbitals. The apparently metallic Ta_4 clusters are at odds with local Jahn-Teller mechanisms generally accepted as the origin of structural transitions in Lacunar spinels and evidence that a picture from mean field arguments for M_4 molecular clusters should be revisited, especially in the case of Ta and Nb compounds [35–37]. For $GaTa_4Se_8$, a minimal description should involve active and hybridized Ta and Se molecular orbitals on cubane clusters, spin-orbit coupling on the molecular orbitals, as well as interactions between clusters. The mixed character of dynamic distortions and decomposition of the structural transition into a superposition of irreducible representations implicate a degeneracy among possible Jahn-Teller distortions in $GaTa_4Se_8$. This is likely a consequence of spin-orbit couplin, covalency, and configurational mixing on the Ta_4 clusters [36,52]. Ultimately, additional interactions between clusters acting on the scale of T^* select a unique valence bond state and quench the structural fluctuations.

V. DISCUSSION

We find that local and dynamic distortions are present up to at least 300 K in $GaTa_4Se_8$. These reduce tetrahedral
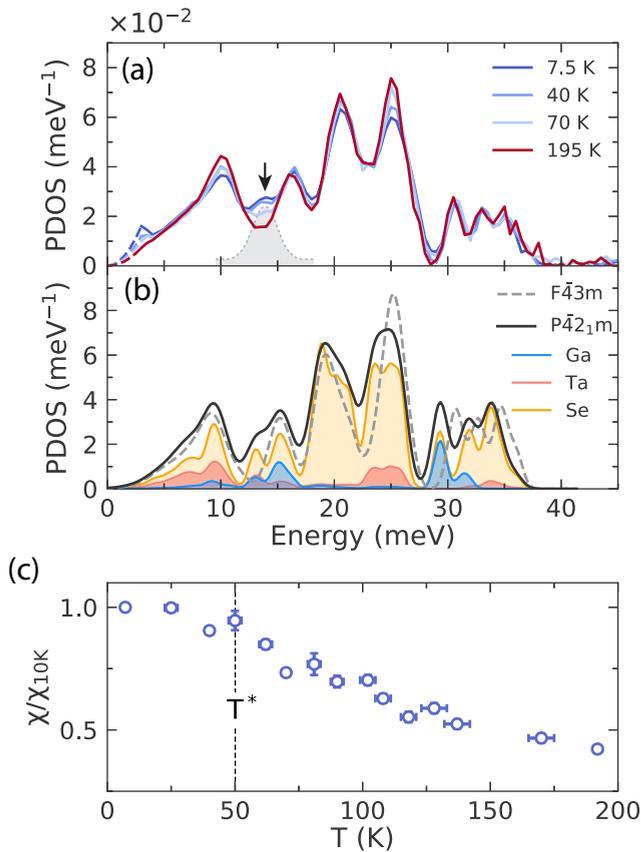
FIG. 5. Dynamic symmetry breaking in $GaTa_4Se_8$. (a) Measured neutron weighted phonon density of states in $GaTa_4Se_8$. A representative Lorentzian fit to the cubic symmetry forbidden optical phonon intensity at 13.8 meV is shown as the gray shaded area. (b) DFT calculated neutron weighted phonon DOS for the cubic ($F\bar{4}3m$) and tetragonal ($P\bar{4}2_1m$) cells. Partial contributions to the tetragonal cell DOS are also shown. (c) Temperature dependence of the 13.8-meV intensity extracted from Lorentzian fits to the dynamic susceptibility.

symmetry of the Ta_4 clusters and dynamically break orbital degeneracy. Heat capacity measurements have found an entropy change associated with T^* approaching $\ln(4)$ [26,27] indicating that the orbital and spin degrees of freedom simultaneously freeze-out at T^*. In other words, T^* corresponds to a collective, order-disorder, spin-orbital ordering between two insulating phases. A discrete sixfold rotational symmetry on the FCC lattice is broken through T^* and we propose this order is selected through intercluster spin-orbital interactions that act on the scale of T^*.

Interestingly, diffraction measurements indirectly implicate dynamic structural fluctuations above global structural transitions in other lacunar spinels [25,28,40]. However, the nature of structural and magnetic transitions, local distortions of transition metal clusters, low-temperature crystal structure, and magnetic state are unique in $GaTa_4Se_8$ among the family of d^1 Lacunar spinels. $GaV_4(S,Se)_8$ and $GaNb_4Se_8$ exhibit a typical separation of spin and orbital energy scales with rhombahedral structural distortions that quench orbital moments occurring at high temperatures preceding lower-temperature spin only magnetic transitions [17,19,24,26,40,53]. $GaNb_4S_8$

exhibits a unit cell doubling spin-orbital transition that is similar to $GaTa_4Se_8$, but the symmetry of the low-temperature structure is further reduced from $P\bar{4}2_1m$ to $P2_12_12_1$ with Nb_4 clusters distorting along cubic body diagonal directions in an antiferro pattern [20,28,54]. The material trend implicates both spatially extended electron density and spin orbit coupling as these both increase from $V \rightarrow Nb \rightarrow Ta$ and can respectively act to drastically alter Jahn-Teller physics [8,55]. In particular, for $j = 3/2$ degrees of freedom, spin orbit coupling can lead to a degeneracy among different types of possible Jahn-Teller distortions [8]. The symmetry forbidden phonon intensity we observe above T^* in $GaTa_4Se_8$ is consistent with such a degeneracy that is ultimately broken by additional interactions.

Above T^*, $GaTa_4Se_8$ is a correlated Mott insulator [32,33], containing an odd number of electrons in the cubic cell. While the Tetragonal unit cell below T^* contains four formula units and an even number of valence electrons, our band structure calculations find a metallic state for this structure, supporting the Mott insulating picture. The absence of magnetic ordering must then indicate a valence bond solid type ground state. The structural dimerization suggests a staggered valence bond covering shown in Fig. 1(b). Such a sharp reduction in magnetic susceptibility and dimerized superstructure below T^* is remarkably similar to the orbitally induced Peierls metal-insulator transitions observed in spinels [6,7,56] and other orbitally degenerate compounds exhibiting temperature-dependent metal insulator transitions [57,58]. However, in $GaTa_4Se_8$ the transition is between two insulating states.

Resonant inelastic x-ray scattering found that at the level of DFT the molecular orbital state in $GaTa_4Se_8$ is molecular analog of the atomic $j = 3/2$ [30]. Although, covalency, configurational interactions between molecular orbitals, and local distortions alter the pure $j = 3/2$ description [36,37,52], it may still stand as an approximate description of the magnetism. In this case $GaTa_4Se_8$ may realize a spin-orbital dimer ground state proposed for Mott insulators on an FCC lattice with d^1 filling and large spin-orbit coupling [11]. Our measurement show how the lattice degrees of freedom can act to select an ordered valence bond solid from the glassy spin-orbit dimer covering proposed in Ref. [11].

Our measurements implicate an essential role played by cluster orientational ordering to affect a Peierls like intercluster dimerization at T^*. This ordering is likely driven by intercluster spin-orbit interactions that break the degeneracy of orbital configurations. The importance of such interactions is further underscored by the primary involvement of both Ta and Se ions across intercluster bonds through the structural transition. Despite the large intercluster separation, closest Ta-Ta distance 4.274 Å closest Ta-Se distance 2.744 Å, there is strong evidence that intercluster exchange is a relevant energy scale in lacunar spinels. For example, recent inelastic neutron-scattering measurements of spin waves in magnetically ordered GaV_4S_8 suggest exchange interactions between the clusters on the order of 20 K [59]. A more spatially extended electron density on Ta $5d$ orbitals should give rise to enhanced interactions compared with the V compounds so that exchange interactions on the scale of $T^* = 50$ K are not unreasonable. In $GaTa_4Se_8$ the broken symmetry at

T^* involves both spin and orbital degrees of freedom and such spin-orbital exchange may be mediated through lattice vibrations [60,61]. The 13-meV mode we observe distorts Ta_4 clusters, simultaneously modulating orbital occupancy, intercluster distances, and Ta-Se bond angles to influence intercluster interactions. In this respect, the optical phonon response we observe in $GaTa_4Se_8$ is reminiscent of spin Peierls compound $CuGeO_3$ [62,63], but in the case of $GaTa_4Se_8$, lattice vibrations affect a complex spin-orbital exchange. Further theoretical effort investigating the role of optical phonons in generating effective spin-orbital interactions in cluster Mott insulators is required [64,65]. Our results provide empirical insight on the microscopic mechanisms that may generate such orbital interactions.

In summary, we have used a combination of single crystal diffraction, total scattering, and inelastic neutron-scattering measurements to show that Ta_4 tetrahedral clusters in $GaTa_4Se_8$ are locally and dynamically distorted up to temperatures of at least 300 K. We resolve the optical phonon modes associated with lattice fluctuations between degenerate orbital configurations on the FCC lattice. We propose that the degeneracy of these configurations is broken through intercluster spin-orbit exchange interactions. A collective order-disorder spin-orbital transition in $GaTa_4Se_8$ is characterized by the long range orientational ordering of distorted Ta_4 clusters to form weak structural dimers aligned along $\langle 110 \rangle$ directions. This suggests that a spin-orbital valence bond solid ground state may be realized in $GaTa_4Se_8$.

APPENDIX A: METHODS

1. Sample synthesis

Single crystal samples of $GaTa_4Se_8$ were synthesized by solid-state reaction. About 1.5 g of stoichiometric quantities of Ga, Ta, and Se were loaded into a I.D. $= 10$ mm, 170 mm long quartz ampules under an argon glovebox, evacuated, and sealed. The ampules were heated to 1050 °C with 80 °C/h ramping rate and stayed at 1050 °C for 24 h. Then cooled to 850 °C with 1 °C/h cooling rate before air quenching. We were able to obtain thousands of high-quality single crystals with a dimension above 200 microns in a single batch. The quality of single crystals was confirmed by x-ray diffraction (Ag Kα radiation). The composition was confirmed by powder x-ray diffraction with ground crystals (Bruker Cu Kα radiation).

2. Synchrotron x-ray crystallography

Temperature-dependent synchrotron x-ray diffraction measurements were carried out on the QM2 beamline at Cornell High Energy Synchrotron source using an x-ray energy of 20.67 keV (0.5998 Å), and the Pilatus 300K area detector positioned 56.2 cm from the sample. The single crystal sample was mounted on a Cu post on the coldfinger of a closed cycle cryostat for measurements in reflection geometry between 3 and 300 K.

Synchrotron x-ray crystallography measurements were carried out on 15-ID at Advanced Photon Source, Argonne National Laboratory using an x-ray energy of 30.00 keV (0.4133 Å) and Pilatus CdTe detector positioned at 7 cm from the sample. The 20-μm single crystal was mounted on a quartz capillary, and measurements were carried out between 10 K and 300 K using a He cryostream. Diffraction peaks were indexed, the unit cell, and UB matrix of each tetragonal domain were determined in reciprocal lattice and **CELLNOW** software for six domains. All frames were integrated using Bruker **SAINT** software, and multidomain absorption corrections were performed through **TWINABS**. The crystal structure was solved by direct methods and least-square method refinements on F^2 were carried out using **SHELXTL** [66] and **Olex2** [67] packages. The converged solution using full single domain reflection data and all Ga, Ta and Se atoms were modeled by isotropic atomic displacement parameters. We checked $1 \times 1 \times 2$, $2 \times 2 \times 1$ and $2 \times 2 \times 2$ superlattices in -4 and $-42m$ tetragonal lattice classes. Based on the extinction rules of x-ray reflection, we find the P$\bar{4}2_1m$ space group with $1 \times 1 \times 2$ superlattice is the most consistent with our data. Details of the crystallographic analysis are provided Appendix B.

3. Pair distribution function measurements

Synchrotron total scattering measurements (xPDF) were conducted on 28-ID-1 (PDF) beamline at the National Synchrotron Light Source-II at Brookhaven National Laboratory. The sample was loaded in a 1 mm I.D. kapton capillary, mounted in a He cryostat, and data was collected between 5 K and 330 K on warming in 5 K steps. Measurements were carried out using an x-ray energy of 74.46 keV (0.1665 Å). We used an amorphous silicon PerkinElmer area detector with a
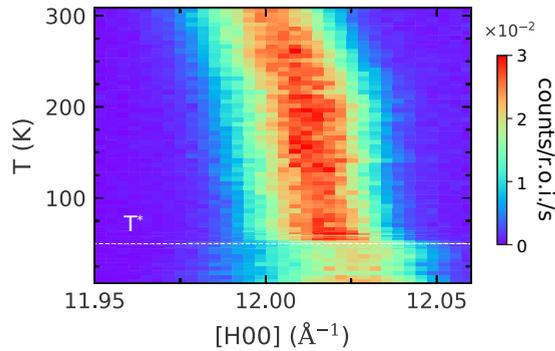
FIG. 6. Temperature-dependent longitudinal cut through [12, 0, 0] reflection. The peak shows a sudden broadening across T^*, indicating a cubic to tetragonal structural transition.

sample to detector distance of 1008 mm for diffraction and 204 mm for PDF. Detector position was determined by calibration using a Ni standard. The two-dimensional diffraction data were integrated using PyFAI [68] and then corrected, normalized, and Fourier transformed to obtain the atomic pair distribution function (PDF), $G(r)$, using PDFgetX3 [69] and a $Q_{max} = 27 \text{ Å}^{-1}$.

Neutron total scattering measurements (nPDF) were carried out on the NOMAD beamline at Spallation Neutron Source at Oak Ridge National Laboratory. A 4.2-g sample was loaded into a vandadium sample can and mounted on the coldfinger of a He cryostat. Data was collected for 160 minutes at 5 K, 55 K, and 300 K, and 80 minutes for intermediate temperatures. The structure factor $S(Q)$ was checked to determine the Q_{max} for each temperature. Background subtracted time-of-flight data were reduced and transformed to PDF using a $Q_{max} = 34.5 \text{ Å}^{-1}$ and ADDIE available at NOMAD [70]. xPDF and nPDF refinements were carried out using PDFgui and DIFFPY − CMI modeling platforms [71].

4. Inelastic neutron scattering

Inelastic neutron-scattering measurements were carried out on the SEQUIOA spectrometer at the Spallation Neutron Source at Oak Ridge National Laboratory. A 5-g polycrystalline sample was loaded into an Al sample can and mounted on the coldfinger of a closed cycle cryostat to achieve a base temperature of 5 K. Measurements were conducted using a fixed incident energy $E_i = 60$ meV and the coarse Fermi chopper rotating at 300 Hz, providing an energy resolution at the elastic line of 3.1 meV. All data were normalized and reduced using algorithms in the MANTID analysis software [72]. The normalized neutron intensities were converted into neutron weighted phonon density of states by integrating over Q (0.2 to 5 Å^{-1}) and corrected for multiphonon and multiscattering processes within the incoherent approximation [73].

APPENDIX B: CRYSTAL STRUCTURE SOLUTION

We performed temperature-dependent x-ray diffraction measurements on a four-circle geometry diffractometer in our laboratory at Brown University. We used a microfocused Ag Kα x-ray source and collected the data using a GaAs photon counting area detector (256 × 256 pixels) with 55 × 55 μm^2
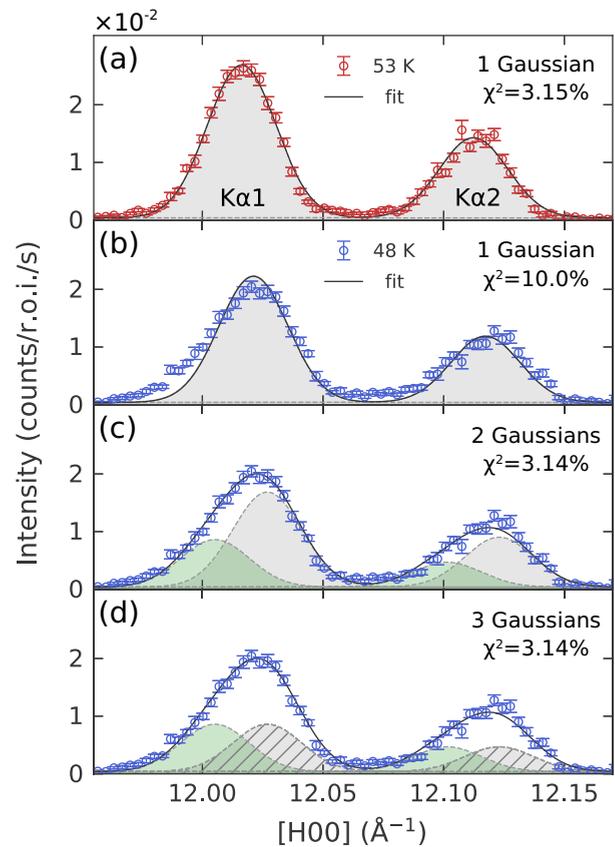

FIG. 7. Gaussian fits above, and below T^* on [12, 0, 0] reflection. (a) $T = 53$ K, the widths of Kα1 and Kα2 reflections are constrained. In (b), (c), and (d), $T = 48$ K, the widths of Gaussians were fixed to the fitted width at $T = 53$ K. (b) Single Gaussian for each Kα1 and Kα2 reflection. (c) Two-Gaussian fit with 2:1 peak intensities for tetragonal scenario. (d) Three-Gaussian fit with 1:1:1 peak intensities for orthorhombic scenario. Two Gaussians overlap in the hatched area.

pixel size. The temperature dependence of a [12, 0, 0] longitudinal scan and representative fits are shown in Figs. 6 and 7, respectively. Our laboratory based Ag x-ray source contains contributions from two wavelengths, Ag Kα_1 (0.5594 Å) and Kα_2 (0.5638 Å), these cannot be separated by our focusing optics, but the Bragg reflections from each wavelength are spatially resolved on our area detector so that the contribution from each wavelength can be fit simultaneously. Scans at select temperatures above T^* are shown in Fig. 6. The peak widths are consistent above T^*, but abruptly increase below 50 K. Peaks were fit with single, double, and triple Gaussians with constrained peak widths at 52 K ($\sigma = 0.01399$), shown in Fig. 7. Data below T^* are most consistent with two Gaussian components with a 2:1 relative intensity, indicative a cubic-tetragonal structural transition, shown in Fig. 2(c) of the main text.

Representative two-dimensional slices from data used for crystallographic refinement are shown in Figs. 8(a) and 8(b). The space-group of the low-temperature structure can be constrained by examining the systematically absent reflections for a tetragonal cell. Body-centered tetragonal space groups are ruled out by the appearance of reflections with h+k+l ≠
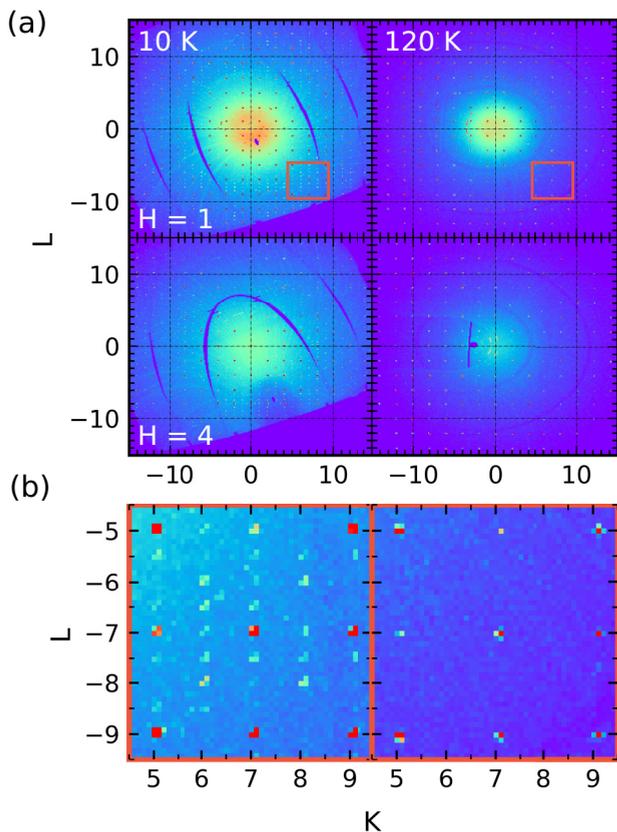
FIG. 8. (a) Crystallographic measurements at 10 K and 120 K. $H = 1$ and $H = 4$ K-L slices are shown. Below T^*, superlattice peaks at half-integer positions appeared. (b) Magnified figures for the red box areas in (a).

2n, indexed in the tetragonal cell. The absence of [h, 0, 0], h = 2n+1, rules out all primitive tetragonal space groups excepting $P\bar{4}2_1m$. Accordingly, $P\bar{4}2_1m$ is the most plausible space group for the low-temperate structure, which is also a maximal subgroup of $F\bar{4}3m$ with a given unit cell doubled tetragonal structure. Multiple twin laws and intensity corrections are necessary for crystallographic refinement to account for nonmerohedral twidding of the tetragonal cell. We followed general procedures used for other systems with non-Merohedral twinning [74]. We applied three twin laws:
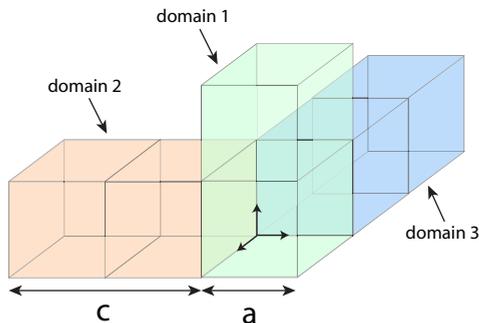

FIG. 9. Twin laws of low-temperature structure. Each domain has its inversion domain; therefore, there are six domains at low temperatures.
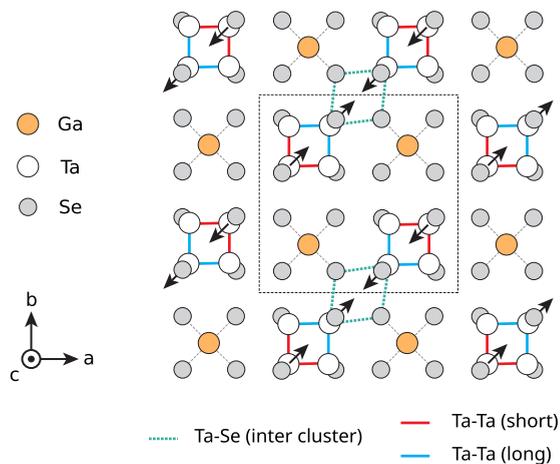

FIG. 10. The refined structure shows distorted Ta_4 clusters and the formation of cluster dimers below T^*. Arrows indicate the shifts of Ta atoms along $\langle 110 \rangle$ direction.

(1) Original tetragonal cell (2) rotate (1) against [1, 0, 0] axis with $-90°$ (3) rotate (1) against [0, 1, 0] with $-90°$, as shown in Fig. 9. For each domain, we applied an additional inversion twin law to account for the inversion twinning. Therefore, six domains are considered in our crystallographic analysis. The peak intensities were integrated by Bruker SAINT software with multiple domains, and the domain population determined using the TWINABS package based on 4/mmm symmetry and $P\bar{4}2_1m$ space group. Finally, we used a total of 13 104 reflections (single domain) for structure refinement with SHELXL [66] and Olex2 [67]. We were not able to stabilize the structure with full anisotropic thermal parameters, probably due to the disorder of the multidomain structure. As a consequence, within isotropic thermal parameters, we obtained the crystal structure for a single domain that has $R = 8.79\%$, $wR_2 = 10.18\%$ with 99.9% completeness of data set for $P\bar{4}2_1m$ structure. The details of the crystallographic refinement are summarized in Table I of the Supplemental Material [44]. The refined structure displays alternating intercluster distances along $\langle 1 \pm 1 \, 0 \rangle$ direction indicates the formation of cluster dimers (Fig. 10).

1. Primary mode analysis

A primary mode analysis for a $k = (1/2, 0, 0)$ structural transition between $F\bar{4}3m$ and $P\bar{4}2_1m$ space groups described in the main text was performed on the Bilbao crystallographic
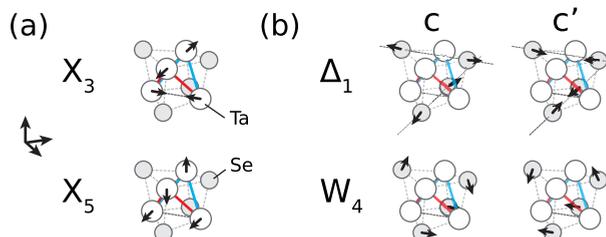

FIG. 11. Primary distortion modes at 10 K. (a) X_3 and X_5 modes. (b) Δ_1 and W_4 modes double the unit cell along c axis. Δ_1 mode produces the large and small Ta_4Se_4 in c and c' layer, respectively.

TABLE I. Intra- and intercluster distances in Å. The definition of bonds are shown in Fig. 19. c and c' denote the inequivalent clusters in $P\bar{4}2_1m$ tetragonal structure. PBE (PAW-PBE) and SOC (PBE+SOC) are optimized structures from DFT.

	PBE (c)	PBE (c')	SOC (c)	SOC (c')	Exp (c)	Exp (c')
l	3.129	3.129	3.084	3.084	3.06	3.04
l'	3.086	3.086	3.053	3.053	3.03	3.03
s'	2.939	2.939	2.951	2.951	2.97	2.97
s	2.927	2.927	2.935	2.935	2.95	2.95
d_l	4.358	4.357	4.331	4.332	4.30	4.29
d_s	4.283	4.282	4.273	4.273	4.28	4.27

server [42,43,75]. Details of mode amplitudes are shown in Fig. 11 and Table II. Atomic displacements are listed in Tables IV– X of the Supplemental Material [44].

APPENDIX C: SUPPORTING DATA FOR PAIR DISTRIBUTION ANALYSIS

In Fig. 12, we compared simulations of the PDF intensity with our neutron PDF results. The thermal parameters at 60 K and 45 K were used for $F\bar{4}3m$ and $P\bar{4}2_1m$ structure, respectively. The instrumental $Q_{broad} = 0.018$ and $Q_{damp} = 0.019$ were used in all simulations. The simulations show that in the large-r regime $F\bar{4}3m$ and $P\bar{4}2_1m$ structures are not distinguishable, except a slight change in peak widths that resembles thermal broadening. To search for this effect in our data, the temperature-dependent thermal parameters were extracted using $F\bar{4}3m$ cubic structure against the large-r regime (30 to 60 Å). In order to minimize the parameter space, we constrained the model to isotropic thermal parameters and assumed each species of atom had the same value. The result shown in in Fig. 13 reveals a small upturn in the Ta thermal parameters across T^*, consistent with expectations from the simulated PDFs.

In order to track the temperature dependence of local distortions independent of any structural model, we fit data in the region $r < 5$ Å to five and six Gaussian functions for xPDF and nPDF, respectively, as shown in Fig. 14. From our fits we extract a normalized PDF intensity $x(r', T)$ shown in Fig. 3. Figure 15 shows the temperature-dependent interatomic distances extracted from the same fits.

TABLE II. Irreducible representation of distortion modes. Amplitudes are normalized with respect to the primative unit cell of the $F\bar{4}3m$ structure.

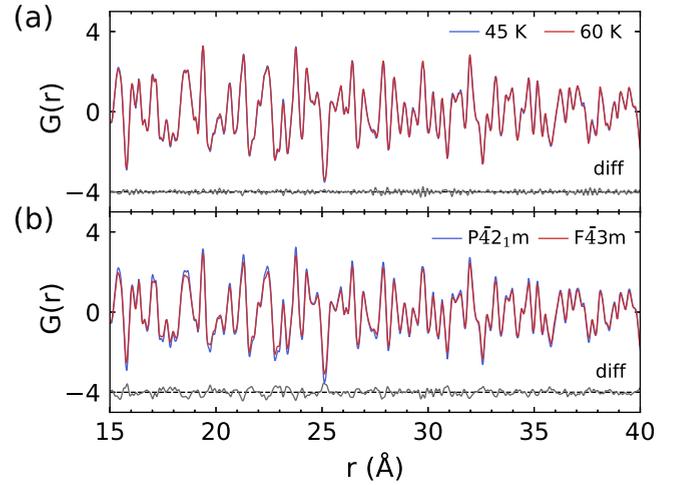| $\vec{K}$	Irrep	Direction	Isotropy SG	Amp. (Å)
$(0,0,0)$	Γ_1	(a)	$F\bar{4}3m$	0.0061
$(0,0,0)$	Γ_3	$(a,0)$	$I\bar{4}m2$	0.0020
$(0,\frac{1}{2},0)$	Δ_1	$(0,0,0,0,a,-a)$	$P\bar{4}m2$	0.0212
$(0,1,0)$	X_3	$(0,a,0)$	$P\bar{4}m2$	0.0719
$(0,1,0)$	X_5	$(0,0,0,a,0,0)$	$P\bar{4}2_1m$	0.1196
$(\frac{1}{2},1,0)$	W_4	$(0,a,0,0,0,0)$	$I\bar{4}2m$	0.0260

FIG. 12. Experimental and simulated PDFs in large-r range. (a) Neutron PDF at 45 K and 60 K. (b) Simulations for $F\bar{4}3m$ and $P\bar{4}2_1m$ structures. $Q_{damp} = 0.018$ and $Q_{broad} = 0.019$ were used for simulations.

APPENDIX D: SUPPORTING DATA FOR INELASTIC NEUTRON SCATTERING AND PHONON MODES

To compare inelastic neutron-scattering data across a large range of temperatures, we weight the measured intensity by the Bose factor and plot a dynamic susceptibility $\chi''(Q, E)$ in in Fig. 16. The 13-meV mode is readily visible in the region highlighted in the dashed box of Fig. 16. Figure 17 shows the representative $\chi''(E)$ integrated over $0.38 < Q < 5.5$ Å^{-1}. We concentrated on data between energy transfers of 9 and 28 meV and found that this region was adequately described by a fit to 5 Gaussian functions with a constant background. Figures 17(b) and 17(c) show the fit results at 7 K and 192 K, respectively. Temperature-dependent phonon mode intensities extracted from the Gaussian fits are shown in Fig. 18(a). All Bose factor corrected phonon mode intensities are con-
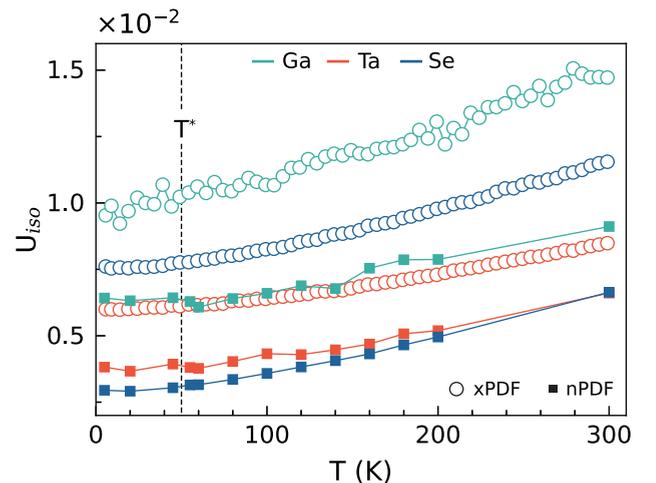

FIG. 13. Thermal parameters extracted from PDF refinements with $F\bar{4}3m$ cubic structure. We only observed a slight upturn in thermal parameters across T^*. The error bars of the fits are within the symbol size.
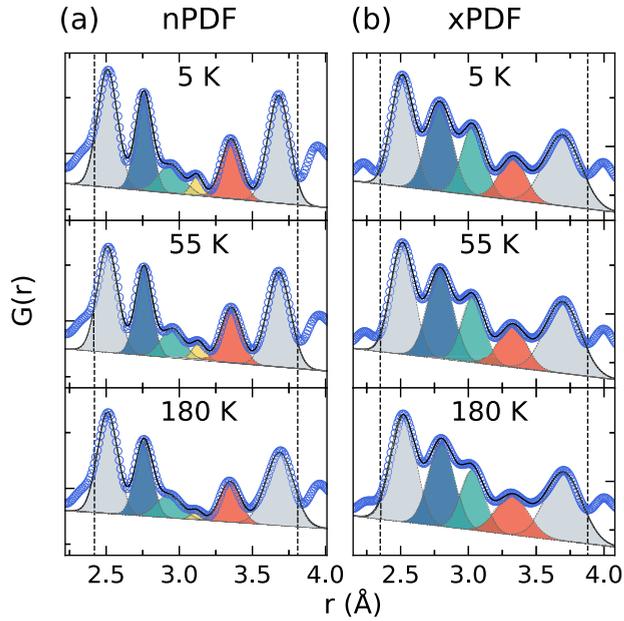
FIG. 14. Representative Gaussian temperature-dependent peak intensity fits at 5 K, 55 K, and 180 K, for (a) nPDF data, and (b) xPDF data.

FIG. 16. Measured dynamic susceptibility $\chi''(Q,E)$ at 192 K, 70 K, 40 K, and 7 K. Dashed boxes highlight the phonon mode at 13 meV.

sistent across measured temperatures except for the 13-meV intensity that displays a prominant temperature dependence. Figure 18(b) shows the temperature-dependent energy and width of 13-meV phonon mode are constant in the measured temperature range.

APPENDIX E: DENSITY-FUNCTIONAL THEORY

1. Electronic structure

We carried out DFT calculations of the electronic structure of P$\bar{4}2_1$m GaTa$_4$Se$_8$ without [Perdew-Burke-Ernzerhof (PBE)] and with spin-orbit coupling (PBE+SOC). We used a 680 eV (PAW-PBE) and 620 eV (PBE+SOC) cutoffs for plane-wave energy with $6 \times 6 \times 6$ (cubic) and $5 \times 5 \times 3$ (tetragonal) Monkhorst-Pack k-point mesh for self-consistent-field calculations. The PAW method [76] and Perdew-Burke-Ernzerhof (PBE) exchange-correlation func-
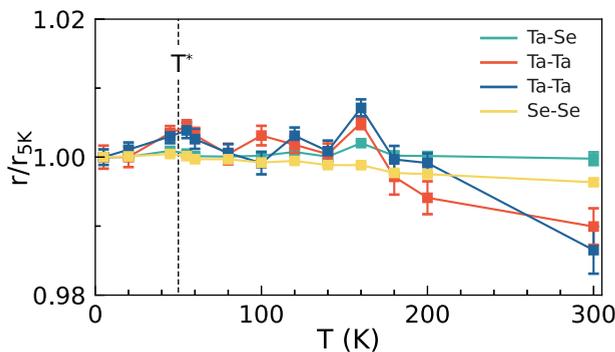

FIG. 15. Temperature-dependent interatomic distances extracted from nPDF. The interatomic distances are normalized by their value at 5 K.
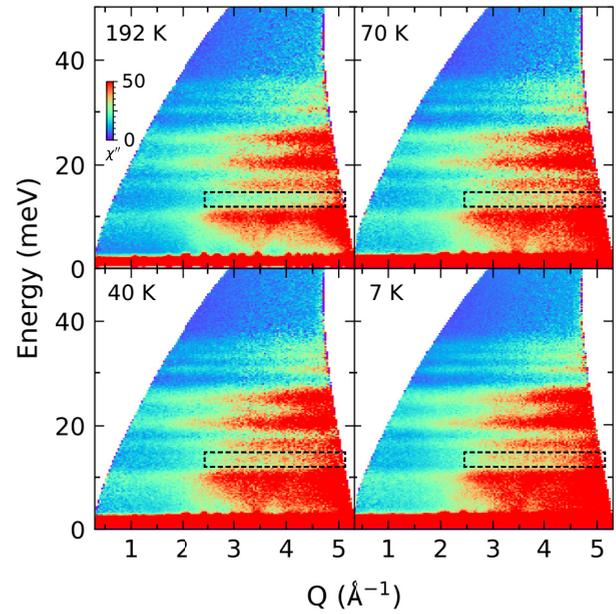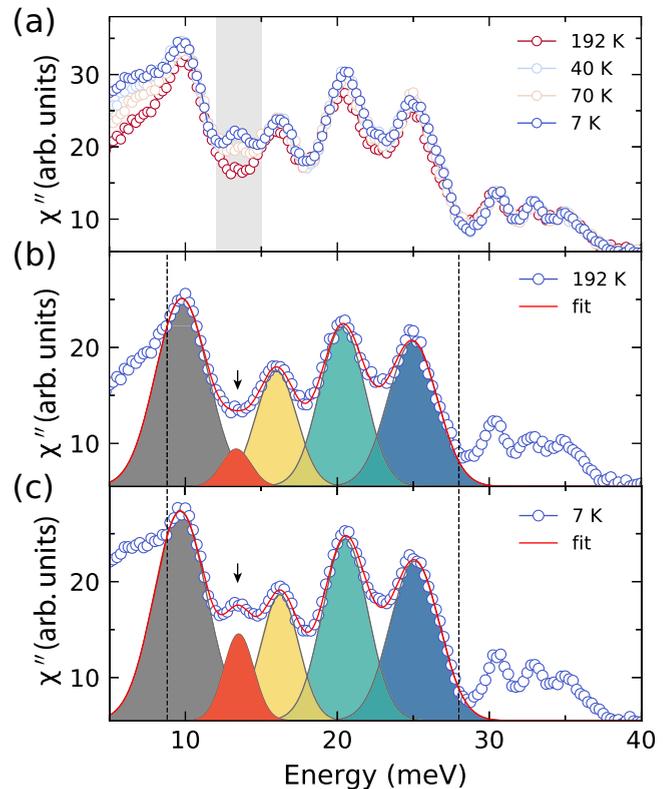

FIG. 17. (a) Temperature-dependent $\chi''(E)$ integrated over $Q = 0.38$ to $5.5\,\text{Å}^{-1}$. (b) The fit for 7 K data. (c) The fit for 192 K data. The shaded area highlights the contribution of 13-meV mode, and two dashed lines indicate the fit range.
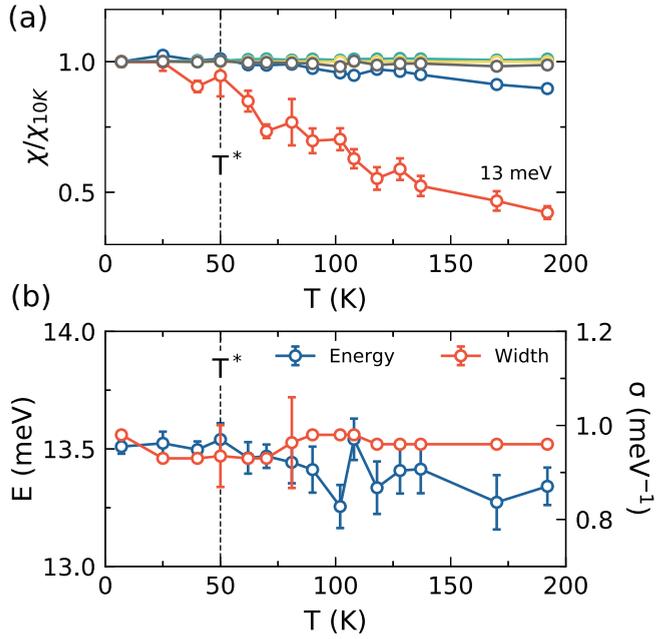
FIG. 18. (a) Temperature-dependent mode intensity. χ is the amplitude of fitted Gaussian. Representative fits are shown in Figs. 17(b) and 17(c). (b) Temperature-dependent energy and width of 13-meV mode. The peak energy and width are fairly consistent in measured temperature range.

tional [77] were used for all calculations. All calculations were performed using Quantum ESPRESSO [78,79]. Cell parameters were restricted by $\bar{P}42_1m$ space group and the force threshold was set to 4×10^{-5} a.u. The criteria of equivalent atomic positions was 1×10^{-5} Å. The optimized structures are consistent with Ta_4 cluster distortions and intercluster dimerizations along $\langle 110 \rangle$ as we observed in x-ray diffraction. Details of the Ta_4 clusters are presented in Fig. 19 and the inter- and intracluster bond lengths for PAW-PBE (PBE), PBE+SOC (SOC), and experimentally determined values are presented in Table I. The optimized structures display a slightly elongated c axis ($c > 2a$), which also agrees with our experimental result. In addition, we find that PAW-PBE overestimated the unit cell size ($a = 10.4677$ Å, $c = 21.0086$ Å) as PBE+SOC ($a = 10.3988$ Å, $c = 20.8129$ Å)
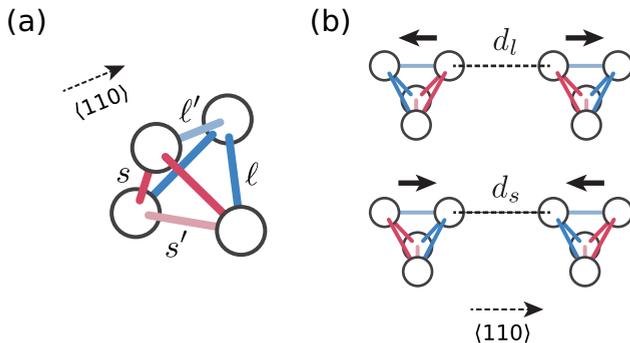

FIG. 19. (a) Local distortion of Ta_4 clusters, $s < s' < l' < l$. (b) The intercluster distances. The bond lengths for the two inequivalent small clusters c and c' are shown in Table I.
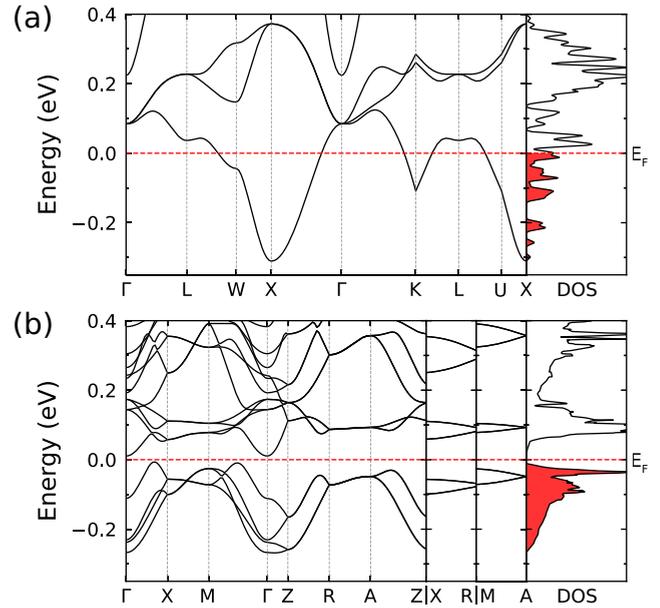

FIG. 20. Electronic structure of $GaTa_4Se_8$ without SOC. (a) Cubic structure ($F\bar{4}3m$, $a = 10.3849$ Å). (b) Tetragonal structure ($\bar{P}42_1m$, $a = 10.4677$ Å, $c = 21.0086$ Å). In tetragonal structure the electronic density of states is reduced at the Fermi level and opens a small gap below T^*.

has smaller cell and slightly closer to experimentally determined values ($a = 10.3437$ Å, $c = 20.6878$ Å). Ta_4 clusters form dimers along $\langle 110 \rangle$ directions in both calculated structures.

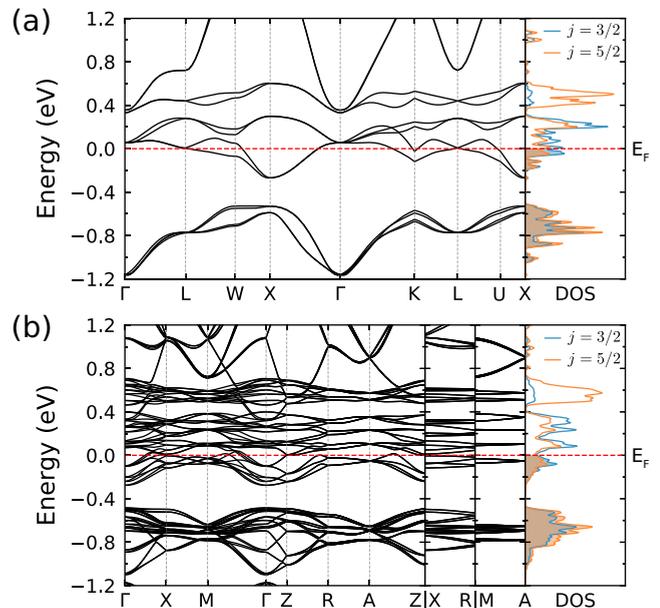FIG. 21. Electronic structure of $GaTa_4Se_8$ with SOC, with the density of states projected into atomic $j = 3/2$ and $j = 5/2$ basis shown in the side panel. (a) Cubic structure ($F\bar{4}3m$, $a = 10.3260$ Å). (b) Tetragonal structure ($\bar{P}42_1m$, $a = 10.3988$ Å, $c = 20.8129$ Å). Both structures require electronic correlation (U) to open a gap, therefore, retains a Mott insulator below T^*.

Band structures and electronic density of states for PAW-PBE and PBE+SOC calculations are shown in Fig. 20 and Fig. 21. In both calculations, the density of electronic states at the E_F is drastically reduced from that of the cubic cell. Without spin-orbit coupling, the unit cell doubled structure opens a small gap since the total electron count is even in a primitive cell. However, with spin-orbit coupling, the splitting of the electronic bands retains a metallic state in the unit cell doubled structure. A large Coulomb interaction, U, is required to open an insulating gap and our band structure calculations indicate that $GaTa_4Se_8$ is retains its Mott insulating nature at low temperatures.

2. Phonon calculations

We used Phonopy package [80] for *ab initio* phonon calculations and Quantum ESPRESSO [78,79] as the force calculator. For phonon calculations, we used 680-eV cutoff for plane-wave energy with a $2 \times 2 \times 1$ Monkhorst-Pack k-point mesh for self-consistent-field calculations. We checked the total energy convergence with the cutoff energy and k-point mesh for calculations. The minimal k-point were used for the cell with 104 atoms. To compare with the results measured by inelastic neutron scattering, the neutron weighted phonon

DOS was calculated

$$PDOS(E) = \sum_i \sigma_i g_i(E), \quad (E1)$$

where σ_i and $g_i(E)$ are neutron cross section and projected phonon density of states for each atomic species. To simulate the measured PDOS, we convolved the calculated PDOS with an empirical instrumental resolution function for SEQUOIA [81]

$$f(E) = 1.435 \times 10^{-6} \times E^3 + 3.885 \times 10^{-4} \times E^2$$
$$- 7.882 \times 10^{-2} \times E + 4.295.$$

The irreducible representation of phonon modes can be calculated with the information of occupied Wyckoff positions (WPs). In $P\bar{4}2_1m$ tetragonal structure, Ga atoms occupy $4e$ WPs. Ta and Se atoms are on $4e$ and $8f$ WPs. Each atom on $4e$ site has $2A_1 + A_2 + B_1 + 2B_2 + 3E$ optical phonon modes, and $3A_1 + 3A_2 + 3B_1 + 3B_2 + 6E$ for atoms on $8f$ WPs. Therefore, the entire unit cell with 20 asymmetric atoms has $46A_1 + 32A_2 + 32B_1 + 46B_2 + 78E$ optical modes. As Fig. 5 in main text shows, the most distinguishable difference between cubic and tetragonal structure is the modes around 13 meV. From our DFT calculation, we assigned phonon modes between 12 and 14 meV to irreducible representation $2A_1 + 2A_2 + 2B_1 + 3B_2 + 4E$, which is the mixed modes of all Ga, Ta and Se atoms.

---

[1] L. F. Feiner, A. M. Oles, and J. Zaanen, Quantum Melting of Magnetic Order Due to Orbital Fluctuations, Phys. Rev. Lett. **78**, 2799 (1997).

[2] H. F. Pen, J. van den Brink, D. I. Khomskii, and G. A. Sawatzky, Orbital Ordering in a Two-Dimensional Triangular Lattice, Phys. Rev. Lett. **78**, 1323 (1997).

[3] S. Di Matteo, G. Jackeli, C. Lacroix, and N. B. Perkins, Valence-Bond Crystal in a Pyrochlore Antiferromagnet with Orbital Degeneracy, Phys. Rev. Lett. **93**, 077208 (2004).

[4] G. Jackeli and D. I. Khomskii, Classical Dimers and Dimerized Superstructure in an Orbitally Degenerate Honeycomb Antiferromagnet, Phys. Rev. Lett. **100**, 147203 (2008).

[5] P. G. Radaelli, D. E. Cox, M. Marezio, and S.-W. Cheong, Charge, orbital, and magnetic ordering in $La_{0.5}Ca_{0.5}MnO_3$, Phys. Rev. B **55**, 3015 (1997).

[6] M. Schmidt, W. Ratcliff, P. G. Radaelli, K. Refson, N. M. Harrison, and S. W. Cheong, Spin Singlet Formation in $MgTi_2O_4$: Evidence of a Helical Dimerization Pattern, Phys. Rev. Lett. **92**, 056402 (2004).

[7] D. I. Khomskii and T. Mizokawa, Orbitally Induced Peierls State in Spinels, Phys. Rev. Lett. **94**, 156402 (2005).

[8] S. V. Streltsov and D. I. Khomskii, Jahn-Teller Effect and Spin-o Coupling: Friends or Foes? Phys. Rev. X **10**, 031043 (2020).

[9] G. Chen, R. Pereira, and L. Balents, Exotic phases induced by strong spin-orbit coupling in ordered double perovskites, Phys. Rev. B **82**, 174440 (2010).

[10] G. Jackeli and G. Khaliullin, Magnetically Hidden Order of Kramers Doublets in $d1$ Systems: Sr_2VO_4, Phys. Rev. Lett. **103**, 067205 (2009).

[11] J. Romhányi, L. Balents, and G. Jackeli, Spin-Orbit Dimers and Noncollinear Phases in d^1 Cubic Double Perovskites, Phys. Rev. Lett. **118**, 217202 (2017).

[12] L. Cianchi, M. Mancini, and P. Moretti, Influence of covalency in the dynamic Jahn-Teller effect in Al_2O_3:Ti3, Phys. Rev. B **7**, 5014 (1973).

[13] M.-H. Whangbo, H.-J. Koo, A. Villesuzanne, and M. Pouchard, Effect of metal-oxygen covalent bonding on the competition between Jahn-Teller distortion and charge disproportionation in the perovskites of high-spin d^4 metal ions $LaMnO_3$ and $CaFeO_3$, Inorg. Chem. **41**, 1920 (2002).

[14] T. Zeng, D. G. Fedorov, M. W. Schmidt, and M. Klobukowski, Effects of spin-orbit coupling on covalent bonding and the Jahn-Teller effect are revealed with the natural language of spinors, J. Chem. Theory Comput. **7**, 2864 (2011).

[15] J. P. Attfield, Orbital molecules in electronic materials, APL Mater. **3**, 041510 (2015).

[16] H. B. Yaich, J. C. Jegaden, M. Potel, M. Sergent, A. K. Rastogi, and R. Tournier, Nouveaux chalcogénures et chalcohalogénures à clusters tétraédriques Nb4 ou Ta4, J. Less-Common Met. **102**, 9 (1984).

[17] R. Pocha, D. Johrendt, and R. Pöttgen, Electronic and structural instabilities in GaV_4S_8 and $GaMo_4S_8$, Chem. Mater. **12**, 2882 (2000).

[18] M. M. Abd-Elmeguid, B. Ni, D. I. Khomskii, R. Pocha, D. Johrendt, X. Wang, and K. Syassen, Transition from Mott Insulator to Superconductor in $GaNb_4Se_8$ and $GaTa_4Se_8$ Under High Pressure, Phys. Rev. Lett. **93**, 126403 (2004).

[19] R. Pocha, D. Johrendt, B. Ni, and M. M. Abd-Elmeguid, Crystal structures, electronic properties, and pressure-induced super-

conductivity of the tetrahedral cluster compounds $GaNb_4S_8$, $GaNb_4Se_8$, and $GaTa_4Se_8$, J. Am. Chem. Soc. **127**, 8732 (2005).

[20] S. Jakob, H. Muller, D. Johrendt, S. Altmannshofer, W. Scherer, S. Rayaprol, and R. Pottgen, Structural and magnetic transitions in the Mott insulator $GaNb_4S_8$, J. Mater. Chem. **17**, 3833 (2007).

[21] D. Bichler, V. Zinth, D. Johrendt, O. Heyer, M. K. Forthaus, T. Lorenz, and M. M. Abd-Elmeguid, Structural and magnetic phase transitions of the V_4-cluster compound GeV_4S_8, Phys. Rev. B **77**, 212102 (2008).

[22] M. Sieberer, S. Turnovszky, J. Redinger, and P. Mohn, Importance of cluster distortions in the tetrahedral cluster compounds GaM_4X_8 (M = Mo, V, Nb, Ta; X = S, Se): *Ab initio* investigations, Phys. Rev. B **76**, 214106 (2007).

[23] A. Camjayi, R. Weht, and M. J. Rozenberg, Localised wannier orbital basis for the mott insulators GaV_4S_8 and $GaTa_4Se_8$, Europhys. Lett. **100**, 57004 (2012).

[24] V. Malik, C. S. Yadav, A. Rastogi, and D. Kumar, Peculiar magnetism of transition metal cluster compounds, Europhys. Lett. **101**, 67008 (2013).

[25] T. Waki, Y. Kajinami, Y. Tabata, H. Nakamura, M. Yoshida, M. Takigawa, and I. Watanabe, Spin-singlet state formation in the cluster mott insulator $GaNb_4S_8$ studied by μSR and NMR spectroscopy, Phys. Rev. B **81**, 020401(R) (2010).

[26] H. Ishikawa, T. Yajima, A. Matsuo, Y. Ihara, and K. Kindo, Nonmagnetic Ground States and a Possible Quadrupolar Phase in 4d and 5d Lacunar Spinel Selenides GaM_4Se_8 (M = Nb, Ta), Phys. Rev. Lett. **124**, 227202 (2020).

[27] S. Kawamoto, T. Higo, T. Tomita, S. Suzuki, Z. M. Tian, K. Mochitzuki, A. Matsuo, K. Kindo, and S. Nakatsuji, Frustrated magnetism in a Mott insulator based on a transition metal chalcogenide, J. Phys.: Conf. Ser. **683**, 012025 (2016).

[28] K. Geirhos, J. Langmann, L. Prodan, A. A. Tsirlin, A. Missiul, G. Eickerling, A. Jesche, V. Tsurkan, P. Lunkenheimer, W. Scherer, and I. Kézsmárki, Cooperative Cluster Jahn-Teller Effect as a Possible Route to Antiferroelectricity, Phys. Rev. Lett. **126**, 187601 (2021).

[29] H.-S. Kim, J. Im, M. J. Han, and H. Jin, Spin-orbital entangled molecular jeff states in lacunar spinel compounds, Nat. Commun. **5**, 3988 (2014).

[30] M. Y. Jeong, S. H. Chang, B. H. Kim, J.-H. Sim, A. Said, D. Casa, T. Gog, E. Janod, L. Cario, S. Yunoki, M. J. Han, and J. Kim, Direct experimental observation of the molecular Jeff = 3/2 ground state in the lacunar spinel $GaTa_4Se_8$, Nat. Commun. **8**, 782 (2017).

[31] M. Y. Jeong, S. H. Chang, H. J. Lee, J.-H. Sim, K. J. Lee, E. Janod, L. Cario, A. Said, W. Bi, P. Werner, A. Go, J. Kim, and M. J. Han, $J_{eff} = \frac{3}{2}$ metallic phase and unconventional superconductivity in $GaTa_4Se_8$, Phys. Rev. B **103**, L081112 (2021).

[32] V. Ta Phuoc, C. Vaju, B. Corraze, R. Sopracase, A. Perucchi, C. Marini, P. Postorino, M. Chligui, S. Lupi, E. Janod, and L. Cario, Optical Conductivity Measurements of $GaTa_4Se_8$ Under High Pressure: Evidence of a Bandwidth-Controlled Insulator-to-Metal Mott Transition, Phys. Rev. Lett. **110**, 037401 (2013).

[33] A. Camjayi, C. Acha, R. Weht, M. G. Rodriguez, B. Corraze, E. Janod, L. Cario, and M. J. Rozenberg, First-Order Insulator-to-Metal Mott Transition in the Paramagnetic 3d System $GaTa_4Se_8$, Phys. Rev. Lett. **113**, 086404 (2014).

[34] M. J. Park, G. Sim, M. Y. Jeong, A. Mishra, M. J. Han, and SungBin Lee, Pressure-induced topological superconductivity

[35] D. Majumdar and K. Balasubramanian, Theoretical study of the electronic states of Nb_4, Nb_5 clusters and their anions (Nb_4^-, Nb_5^-), J. Chem. Phys. **121**, 4014 (2004).

[36] L. Hozoi, M. S. Eldeeb, and U. K. Rößler, V_4 tetrahedral units in AV_4X_8 lacunar spinels: Near degeneracy, charge fluctuations, and configurational mixing within a valence space of up to 21 d orbitals, Phys. Rev. Research **2**, 022017(R) (2020).

[37] T. Petersen, L. Prodan, V. Tsurkan, H.-A. Krug von Nidda, I. Kézsmárki, U. K. Rößler, and L. Hozoi, How correlations and spin–orbit coupling work within extended orbitals of transition-metal tetrahedra of 4d/5d lacunar spinels, J. Phys. Chem. Lett. **13**, 1681 (2022).

[38] E. Ruff, S. Widmann, P. Lunkenheimer, V. Tsurkan, S. Bordács, I. Kézsmárki, and A. Loidl, Multiferroicity and skyrmions carrying electric polarization in GaV_4S_8, Sci. Adv. **1**, e1500916 (2015).

[39] K. Xu and H. J. Xiang, Unusual ferroelectricity induced by the Jahn-Teller effect: A case study on lacunar spinel compounds, Phys. Rev. B **92**, 121112(R) (2015).

[40] Z. Wang, E. Ruff, M. Schmidt, V. Tsurkan, I. Kézsmárki, P. Lunkenheimer, and A. Loidl, Polar Dynamics at the Jahn-Teller Transition in Ferroelectric GaV_4S_8, Phys. Rev. Lett. **115**, 207601 (2015).

[41] E. Ruff, A. Butykai, K. Geirhos, S. Widmann, V. Tsurkan, E. Stefanet, I. Kézsmárki, A. Loidl, and P. Lunkenheimer, Polar and magnetic order in GaV_4Se_8, Phys. Rev. B **96**, 165119 (2017).

[42] D. Orobengoa, C. Capillas, M. I. Aroyo, and J. M. Perez-Mato, Amplimodes: Symmetry-mode analysis on the Bilbao Crystallographic Server, J. Appl. Crystallogr. **42**, 820 (2009).

[43] J. M. Perez-Mato, D. Orobengoa, and M. I. Aroyo, Mode crystallography of distorted structures, Acta Crystallogr. A **66**, 558 (2010).

[44] See Supplemental Material at http://link.aps.org/supplemental/10.1103/PhysRevResearch.4.033123 for details of crystallographic refinements and primary mode analysis.

[45] P. M. M. Thygesen, C. A. Young, E. O. R. Beake, F. D. Romero, L. D. Connor, T. E. Proffen, A. E. Phillips, M. G. Tucker, M. A. Hayward, D. A. Keen, and A. L. Goodwin, Local structure study of the orbital order/disorder transition in $LaMnO_3$, Phys. Rev. B **95**, 174107 (2017).

[46] X. Qiu, T. Proffen, J. F. Mitchell, and S. J. L. Billinge, Orbital Correlations in the Pseudocubic O and rhombohedral R Hases of $LaMnO_3$, Phys. Rev. Lett. **94**, 177203 (2005).

[47] J.-Q. Yan, J.-S. Zhou, J. G. Cheng, J. B. Goodenough, Y. Ren, A. Llobet, and R. J. McQueeney, Spin and orbital ordering in $Y_{1-x}La_xVO_3$, Phys. Rev. B **84**, 214405 (2011).

[48] J.-Q. Yan, W. Tian, H. B. Cao, S. Chi, F. Ye, A. Llobet, A. Puretzky, Q. Chen, J. Ma, Y. Ren, J.-G. Cheng, J.-S. Zhou, M. A. McGuire, and R. J. McQueeney, Lattice distortion in the spin-orbital entangled state in RVO_3 perovskites, Phys. Rev. B **100**, 184423 (2019).

[49] R. J. Koch, R. Sinclair, M. T. McDonnell, R. Yu, M. Abeykoon, M. G. Tucker, A. M. Tsvelik, S. J. L. Billinge, H. D. Zhou, W. G. Yin, and E. S. Bozin, Dual Orbital Degeneracy Lifting in a Strongly Correlated Electron System, Phys. Rev. Lett. **126**, 186402 (2021).

in the spin-orbit Mott insulator $GaTa_4Se_8$, npj Quantum Mater. **5**, 41 (2020).

[50] L. Yang, R. J. Koch, H. Zheng, J. F. Mitchell, W. Yin, M. G. Tucker, S. J. L. Billinge, and E. S. Bozin, Two-orbital degeneracy lifted local precursor to a metal-insulator transition in $MgTi_2O_4$, Phys. Rev. B **102**, 235128 (2020).

[51] S. Reschke, F. Meggle, F. Mayr, V. Tsurkan, L. Prodan, H. Nakamura, J. Deisenhofer, C. A. Kuntscher, and I. Kézsmárki, Lattice dynamics and electronic excitations in a large family of lacunar spinels with a breathing pyrochlore lattice structure, Phys. Rev. B **101**, 075118 (2020).

[52] H.-S. Kim, K. Haule, and D. Vanderbilt, Molecular mott state in the deficient spinel GaV_4S_8, Phys. Rev. B **102**, 081105(R) (2020).

[53] R. L. Dally, W. D. Ratcliff, L. Zhang, H.-S. Kim, M. Bleuel, J. Kim, K. Haule, D. Vanderbilt, S.-W. Cheong, and J. W. Lynn, Magnetic phase transitions and spin density distribution in the molecular multiferroic system GaV_4S_8, Phys. Rev. B **102**, 014410 (2020).

[54] M. Isobe and Y. Ueda, Observation of phase transition from metal to spin-singlet insulator in $MgTi_2O_4$ with S = 1/2 pyrochlore lattice, J. Phys. Soc. Jpn. **71**, 1848 (2002).

[55] D. I. Khomskii and S. V. Streltsov, Orbital effects in solids: Basics, recent progress, and opportunities, Chem. Rev. **121**, 2992 (2021).

[56] P. G. Radaelli, Y. Horibe, M. J. Gutmann, H. Ishibashi, C. H. Chen, R. M. Ibberson, Y. Koyama, Y.-S. Hor, V. Kiryukhin, and S.-W. Cheong, Formation of isomorphic Ir^{3+} and Ir^{4+} octamers and spin dimerization in the spinel $CuIr_2S_4$, Nature (Lond.) **416**, 155 (2002).

[57] Y. Okamoto, S. Niitaka, M. Uchida, T. Waki, M. Takigawa, Y. Nakatsu, A. Sekiyama, S. Suga, R. Arita, and H. Takagi, Band Jahn-Teller Instability and Formation of Valence Bond Solid in a Mixed-Valent Spinel Oxide $LiRh_2O_4$, Phys. Rev. Lett. **101**, 086404 (2008).

[58] N. Katayama, M. Uchida, D. Hashizume, S. Niitaka, J. Matsuno, D. Matsumura, Y. Nishihata, J. Mizuki, N. Takeshita, A. Gauzzi, M. Nohara, and H. Takagi, Anomalous Metallic State in the Vicinity of Metal to Valence-Bond Solid Insulator Transition in $LiVS_2$, Phys. Rev. Lett. **103**, 146405 (2009).

[59] G. Pokharel, H. S. Arachchige, S. Gao, S.-H. Do, R. S. Fishman, G. Ehlers, Y. Qiu, J. A. Rodriguez-Rivera, M. B. Stone, H. Zhang, S. D. Wilson, D. Mandrus, and A. D. Christianson, Spin dynamics in the skyrmion-host lacunar spinel GaV_4S_8, Phys. Rev. B **104**, 224425 (2021).

[60] J. B. Goodenough, A. Wold, R. J. Arnott, and N. Menyuk, Relationship between crystal symmetry and magnetic properties of ionic compounds containing Mn3+, Phys. Rev. **124**, 373 (1961).

[61] L. F. Chibotaru, V. Z. Polinger, and I. B. Bersuker, Vibronic coupling to T_1 and T_2 vibrations and the Jahn-Teller effect in transition-metal exchange tetraclusters, Theor. Exp. Chem. **23**, 605 (1988).

[62] M. Hase, I. Terasaki, and K. Uchinokura, Observation of the Spin-Peierls Transition in Linear Cu^{2+} (spin-1/2) Chains in an Inorganic Compound $CuGeO_3$, Phys. Rev. Lett. **70**, 3651 (1993).

[63] M. Braden, B. Hennion, W. Reichardt, G. Dhalenne, and A. Revcolevschi, Spin-Phonon Coupling in $CuGeO_3$, Phys. Rev. Lett. **80**, 3634 (1998).

[64] J.-S. Zhou, H. Q. Yin, and J. B. Goodenough, Vibronic superexchange in single-crystal $LaMn_{1-x}Ga_xO_3$, Phys. Rev. B **63**, 184423 (2001).

[65] L. F. Chibotaru, Spin-Vibronic Superexchange in Mott-Hubbard Fullerides, Phys. Rev. Lett. **94**, 186405 (2005).

[66] G. M. Sheldrick, A short history of SHELX, Acta Crystallogr. A **64**, 112 (2008).

[67] O. V. Dolomanov, L. J. Bourhis, R. J. Gildea, J. A. K. Howard, and H. Puschmann, Olex2: A complete structure solution, refinement and analysis program, J. Appl. Crystallogr. **42**, 339 (2009).

[68] G. Ashiotis, A. Deschildre, Z. Nawaz, J. P. Wright, D. Karkoulis, F. E. Picca, and J. Kieffer, The fast azimuthal integration python library: *pyFAI*, J. Appl. Crystallogr. **48**, 510 (2015).

[69] P. Juhás, T. Davis, C. L. Farrow, and S. J. L. Billinge, PDFgetX3: A rapid and highly automatable program for processing powder diffraction data into total scattering pair distribution functions, J. Appl. Crystallogr. **46**, 560 (2013).

[70] M. T. McDonnell, D. P. Olds, K. L. Page, J. C. Neufeind, M. G. Tucker, J. C. Bilheux, W. Zhou, and P. F. Peterson, Addie: Advanced diffraction environment–a software environment for analyzing neutron diffraction data, Acta Crystallogr. Sect. A: Found. Adv. **73**, a377 (2017).

[71] C. L. Farrow, P. Juhas, J. W. Liu, D. Bryndin, E. S. Božin, J. Bloch, T. Proffen, and S. J. L. Billinge, PDFfit2 and PDFgui: Computer programs for studying nanostructure in crystals, J. Phys.: Condens. Matter **19**, 335219 (2007).

[72] O. Arnold, J. C. Bilheux, J. M. Borreguero, A. Buts, S. I. Campbell, L. Chapon, M. Doucet, N. Draper, R. Ferraz Leal, M. A. Gigg, V. E. Lynch, A. Markvardsen, D. J. Mikkelson, R. L. Mikkelson, R. Miller, K. Palmen, P. Parker, G. Passos, T. G. Perring, P. F. Peterson *et al.*, Mantid-data analysis and visualization package for neutron scattering and μSR experiments, Nucl. Instrum. Methods Sec. A **764**, 156 (2014).

[73] J. Y. Y. Lin, F. Islam, and M. Kresh, Multiphonon: Phonon density of states tools for inelastic neutron scattering powder data, J. Open Source Softw. **3**, 440 (2018).

[74] M. Sevvana, M. Ruf, I. Usón, G. M. Sheldrick, and R. Herbst-Irmer, Non-merohedral twinning: from minerals to proteins, Acta Crystallogr. D **75**, 1040 (2019).

[75] C. Capillas, E. Kroumova, M. I. Aroyo, J. M. Perez-Mato, H. T. Stokes, and D. M. Hatch, Symmodes: a software package for group-theoretical analysis of structural phase transitions, J. Appl. Crystallogr. **36**, 953 (2003).

[76] P. E. Blöchl, Projector augmented-wave method, Phys. Rev. B **50**, 17953 (1994).

[77] J. P. Perdew, K. Burke, and M. Ernzerhof, Generalized Gradient Approximation Made Simple, Phys. Rev. Lett. **77**, 3865 (1996).

[78] P. Giannozzi, S. Baroni, N. Bonini, M. Calandra, R. Car, C. Cavazzoni, D. Ceresoli, G. L. Chiarotti, M. Cococcioni, I. Dabo *et al.*, QUANTUM ESPRESSO: A modular and open-source software project for quantum simulations of materials, J. Phys.: Condens. Matter **21**, 395502 (2009).

[79] P. Giannozzi, O. Andreussi, T. Brumme, O. Bunau, M. B. Nardelli, M. Calandra, R. Car, C. Cavazzoni, D. Ceresoli, M. Cococcioni *et al.*, Advanced capabilities for materials mod-

elling with Quantum ESPRESSO, J. Phys.: Condens. Matter **29**, 465901 (2017).

[80] A. Togo and I. Tanaka, First principles phonon calculations in materials science, Scr. Mater. **108**, 1 (2015).

[81] G. E. Granroth, A. I. Kolesnikov, T. E. Sherline, J. P. Clancy, K. A. Ross, J. P. C. Ruff, B. D. Gaulin, and S. E. Nagler, Sequoia a newly operating chopper spectrometer at the SNS, J. Phys.: Conf. Ser. **251**, 012058 (2010).